# Lunar Gravitational Maps From GRAIL Gravity, LRO and Kaguya Topography and 3D Crustal Density

**Blažej Bucha**[1]

[1]Department of Theoretical Geodesy and Geoinformatics, Slovak University of Technology in Bratislava, Radlinského 11, 81005 Bratislava, Slovak Republic, https://orcid.org/0009-0006-1694-1544

**Key Points:**

- Lunar gravitational maps have been derived by combining gravity observed by satellites with gravity modeled from topography and 3D density
- Gravitational potential, vector and tensor are depicted at 250-m resolution at the lunar surface and on its circumscribing sphere
- The maps are applicable for spacecraft navigation, inertial navigation or to study gravity-driven mass movements

Corresponding author: Blažej Bucha, blazej.bucha@stuba.sk

**Abstract**

We present a suite of Lunar Gravitational Maps 2026 (LGM2026) at the resolution of 128 pixels per degree (∼250 m at the equator). The maps show the gravitational potential, vector and tensor globally at the lunar surface and on its circumscribing sphere. Long wavelengths up to 11 km are taken from a spherical-harmonic model derived from the Gravity Recovery and Interior Laboratory mission (GRAIL). The remaining short-scale signals are forward-modeled from the lunar topography, as observed by the Lunar Reconnaissance Orbiter (LRO) and Kaguya spacecraft, while using 3D crustal density. Over most regions, the expected accuracy is 2 mGal in terms of the gravitational vector. Possible applications include near-surface spacecraft navigation, inertial navigation or the establishment of a physically meaningful height system. As a by-product, LGM2026 was converted into an external solid spherical-harmonic expansion of the gravitational potential up to degree 11,519.

## Plain Language Summary

Lunar gravity field models are essential to understand the Moon, its evolution and to enable human activities in its vicinity. Perhaps the most valuable observations of the lunar gravity field are due to the Gravity Recovery and Interior Laboratory (GRAIL) mission. By design, GRAIL could not, however, capture the very fine gravity signals caused by local topography. This paper presents lunar gravitational maps that supplement the GRAIL signals by short-scale gravitational features modeled from the topography and its 3D density. The maps are sampled at 250-m resolution, surpassing GRAIL models at least by a factor of ∼20. This resolution could be reached thanks to the Lunar Reconnaissance Orbiter and Kaguya missions, which mapped the lunar topography at the resolution of a few tens of meters globally. Our maps show the gravitational field at the lunar surface and on a sphere completely encompassing the Moon. Possible applications include spacecraft navigation at low altitudes, prediction of gravitational field quantities or inertial navigation.

## 1 Introduction

Knowledge of the lunar gravity field is essential to understand the interior structure of the Moon (e.g., Wieczorek et al., 2013), for topography mapping (e.g., Barker et al., 2016) or for spacecraft navigation (e.g., Chen et al., 2023). A breakthrough in lunar gravity field mapping was achieved by the Gravity Recovery and Interior Laboratory mission (GRAIL; Zuber et al., 2013). GRAIL satellites were, however, insensitive to gravity features beyond the resolution of a few kilometers (e.g., Wieczorek, 2015). Such fine-scale gravity signals are essential, for instance, for spacecraft navigation at landing sites as demonstrated by the Mars rover Curiosity (Way, 2013). In the context of the lunar gravity field, these short wavelengths originate almost exclusively from the topography and from subsurface mass variations (e.g., Zuber et al., 2013; S. Goossens et al., 2020). They can be therefore predicted from topography by means of Newton's law of gravitation.

Thanks to the Lunar Reconnaissance Orbiter (LRO; Chin et al., 2007) and Kaguya missions (Kato et al., 2010), lunar topography models reached resolutions of a few tens of meters globally (e.g., Barker et al., 2016). They are thus better resolved than GRAIL gravity models by 2 orders of magnitude, making them suitable for short-scale gravity predictions. Supplementing observed gravity with gravity from topography is a well-established methodology (e.g., Tziavos & Sideris, 2013), which, under some variations, has been applied to the Earth (e.g., Pavlis et al., 2012; Hirt et al., 2013; Ince et al., 2020), the Moon (e.g., Hirt & Featherstone, 2012), Mars (e.g., Hirt et al., 2012; Górski et al., 2018) or Venus (e.g., Li et al., 2015). Presently, the most detailed lunar surface gravity model is the Lunar Gravity Model 2011 (LGM2011) with its 1.5-km resolution at the equator (Hirt &

Featherstone, 2012). However, after more than a decade since its release, the data and methodology behind LGM2011 no longer represent the state of the art. First, observations made by LRO since the release of LGM2011 led to improved lunar shape models (e.g., Barker et al., 2016). Second, the topography-induced gravity of LGM2011 assumes constant-density topography, but lateral and 3D density modeling have been increasingly studied (e.g., Wieczorek et al., 2013; Besserer et al., 2014; Han et al., 2014; S. Goossens et al., 2020; Šprlák et al., 2020). Third, on the methodological level, the topography-based component of LGM2011 employs the outdated planar approximation and does not incorporate certain correction terms that were discovered by Rexer et al. (2018) a few years after the release of LGM2011. These recent developments stimulate a compilation of new lunar gravitational maps for the benefit of future Moon-related science and engineering applications.

Taking advantage of the new datasets (Section 2) and modeling techniques (Section 3), we developed a suit of Lunar Gravitational Maps 2026 (LGM2026; Section 4) that surpass previous efforts in several aspects. The maps show the gravitational potential, the gravitational vector and the gravitational tensor over the entire lunar surface and on its circumscribing sphere. The resolution of the maps is 128 pixels per degree (PPD), which corresponds to about ∼250 m at the equator. Finally, the maps are based on the gravity from GRAIL, the topography from LRO and Kaguya, and the crustal density from inversion of GRAIL data. Our accuracy assessment suggests a 2 mGal accuracy of the gravitational vector (1 mGal $= 10^{-5}$ m s$^{-2}$; Section 5). LGM2026 is suitable for applications seeking fine-scale surface gravitational information such as gravity prediction at prospective landing sites or spacecraft navigation (Section 6). As the primary limitation, LGM2026 is not suitable for geophysical and geological interpretations (Section 7).

## 2 Data

Long wavelengths of LGM2026 are taken from the Kaula-constrained spherical-harmonic model GRGM1200B (S. Goossens et al., 2020) up to degree 500 (∼11 km at the equator). GRGM1200B is derived from the primary and extended mission GRAIL data and is expanded up to degree 1200. The rationale behind truncating the model at degree 500 is (a) to avoid using coefficients affected by the Kaula-constraint, (b) to avoid the divergence of spherical harmonics at the lunar topography and (c) to mitigate the noise amplification when evaluating the model at the lunar topography (see Text S3.1 in Supporting Information).

The key short-scale gravitational features beyond degree 500 are derived from topographic and density models. The topography was represented by the LDEM128_PA_pixel_202405 model (briefly LDEM128; Neumann, 2024) at the resolution of 128 PPD. LDEM128 is based on data from the Lunar Orbiter Laser Altimeter (LOLA) onboard LRO and from the Kaguya's Terrain Camera. It is expressed in the Moon's principal axes coordinate system (PA), matching the coordinate system of GRGM1200B. For the spherical-harmonic representation of LDEM128, we used the degree-11,519 model Moon_LDEM128_shape_pa_11519.sh.gz (briefly LDEM128_SH; Wieczorek, 2024). The density was represented by the linear 3D density model of S. Goossens et al. (2020) using the variant with the cap radius of 15° and the degree range 250–650.

## 3 Methods

The long-wavelength component of LGM2026 was obtained by the synthesis of the gravitational potential, the gravitational vector and the gravitational tensor from GRGM1200B up to degree 500. In LGM2026, the gravitational vector and tensor are consistently expressed in the local north-oriented reference frame (see Text S1.1 in Supporting Information).

The short-scale LGM2026 signals were delivered by residual terrain modeling (RTM; e.g., Forsberg & Tscherning, 1981; Torge & Müller, 2012; Tziavos & Sideris, 2013) assuming 3D variable mass density and isostatically uncompensated topography at short scales. The idea is first to form a residual terrain by subtracting long-wavelength topography (here LDEM128_SH up to degree 500) from high-resolution topography (LDEM128), and then to calculate gravitational effects of the residual topography using Newton's integral. RTM can thus be viewed as high-pass filtering of gravity fields implied by high-resolution topographies. After the filtering, the short-scale RTM signals can supplement spherical-harmonic gravity models (here GRGM1200B to degree 500), enhancing their spatial and spectral content. Numerous Earth-related studies proved that RTM reduces the omission error of spherical-harmonic gravity models, in some cases by as much as 80 % (e.g., Hirt et al., 2013; Ďuríčková & Janák, 2016; Grombein et al., 2017). Improvements were also observed with lunar (Hirt & Featherstone, 2012) and martian gravity fields (Hirt et al., 2012; Way, 2013), though with less confidence due to the general lack of high-quality surface gravity observations. Importantly, if the correction terms discovered by Rexer et al. (2018) are applied to RTM, the filtration is exact as we prove in Text S1.3.2 in Supporting Information. The assumption of uncompensated lunar topography at short scales (here beyond degree 500) seems realistic (e.g., Wieczorek et al., 2013), making it possible to approximate fine-scale lunar gravity features by RTM.

If the topography is sampled densely and if the number of evaluation points is large, RTM is computationally challenging given the convolutional character of Newton's integral. In our case, the resolution of LDEM128 is 128 PPD, which means $23{,}040 \times 46{,}080 \approx 10^9$ pixels. On the other hand, the number of LGM2026 points is $\sim 2 \times 10^9$, because LGM2026 shows the lunar gravitational field at the lunar surface and on its circumscribing sphere, both at the 128-PPD resolution. Furthermore, at each evaluation point, LGM2026 provides 10 quantities: the gravitational potential, the 3 elements of the gravitational vector and the 6 elements of the gravitational tensor. Even with high-performance computing resources, efficient algorithms and modeling techniques are needed to tackle this task efficiently.

In our RTM approach (see Text S1.3 in Supporting Information), we assumed a 3D variable density distribution inside the lunar crust. The gravitational effects of this mass distribution were evaluated by combining the spatial-domain gravity-forward modeling method of Lin et al. (2020) and the spectral-domain method of Bucha (2025) (see Text S2 in Supporting Information). This combination avoids the divergence issue of spherical harmonics on the lunar surface yet it benefits from the numerical efficiency of spherical harmonics. The gravitational effects were evaluated by integrating masses all around the lunar surface, so even often neglected contributions from remote residual masses were considered. Finally, we took into account the low-frequency RTM correction (Rexer et al., 2018). At the lunar surface, the magnitude of this correction reaches up to 95 mGal and the root mean square is 4 mGal. The high-frequency RTM correction (ibid.) was not relevant, because our spectral-domain gravity-forward modeling method allowed us to truncate the gravitational effects of LDEM128_SH at the desired degree of 500.

To calculate the surface gravitational maps, both the long-wavelength components from GRGM1200B and the short-scale signals from RTM were evaluated 0.1 m above the lunar topography as represented by LDEM128. The offset of 0.1 m is to avoid issues associated with the singularity of Newton's kernel in the spatial-domain gravity-forward modeling. The maps showing the gravitational field on the circumscribing sphere were evaluated at the constant spherical radius of 1,749 km. This sphere passes outside all gravitating masses.

## 4 Results

The main product of LGM2026 are maps of the lunar gravitational gravitational potential, vector and tensor at the lunar surface and on its circumscribing sphere, both sampled at the 128-PPD spatial resolution (see Figures S1 to S8 in Supporting Information). All maps show quantities of the gravitational field, meaning they do not take into account the centrifugal field or the normal gravity field. The coordinate system adopted for all LGM2026 spatial data is the Moon's principal axes coordinate system.

To demonstrate LGM2026, we selected the south polar region, because it is significant for lunar exploration due to the possible presence of water ice (e.g., Fisher et al., 2017; McClanahan et al., 2024). This is also the region where 13 candidate Artemis locations have been identified for possible human landing. Figure 1 shows the gravitational acceleration (magnitude of the gravitational vector) over this area as predicted by LGM2026, LGM2011 and the spherical-harmonic model GRGM1200B + RM1, $\lambda = 1$ to degrees 500 and 900. Two deficiencies of the spherical-harmonic model are clearly visible. If its truncation degree is low, the omission error causes the wavy pattern in Figure 1c. If the truncation degree is high, the signal is overwhelmed by the noise and by the divergence of spherical harmonics which leads to spurious oscillations in Figure 1d. By comparison, LGM2026 (Figure 1a) and LGM2011 (Figure 1b) do not suffer from these effects, as they model also the high-frequency gravitational signals and do not rely on spherical harmonics in short scales. Figure 1e shows the gravitational acceleration at the 13 candidate Artemis sites as determined by the 4 models. Over most stations, LGM2011 predicts largest gravitational acceleration and GRGM1200B + RM1, $\lambda = 1$ to degree 500 yields the lowest value. LGM2026 predictions are typically in between LGM2011 and GRGM1200B + RM1, $\lambda = 1$ to degree 900. A possible explanation for the systematically largest values in LGM2011 could be its constant density of 2800 kg $m^{-3}$ (the surface density in LGM2026 varies from $\sim$2375 to $\sim$2495 kg $m^{-3}$ over this region and increases with depth) or the pre-GRAIL spherical-harmonic gravitational model SGM100i (S. Goossens et al., 2011) used in LGM2011 to degree 70. In the absence of observed surface gravitational data, it is impossible to assess which of the 4 models performs the best in the south polar region. It can be concluded though that the predictions of the gravitational acceleration at the 13 candidate Artemis sites differ by 104 mGal at maximum and that the degree-900 spherical-harmonic model features artificial oscillations over low-elevated topography.

Data published along with LGM2026 include (a) the 3D position of the LGM2026 data points, (b) spherical-harmonic coefficients of the lunar gravitational potential up to degree 11,519 (see Text S5.1 in Supporting Information) and (c) maps of the residual gravitational field beyond degree 500.

## 5 Accuracy

We validated the LGM2026 maps on the circumscribing sphere with respect to the GRAIL-based model GRGM1200B + RM1, $\lambda = 1$ (shortened to GRGM1200B in this section). Unlike its Kaula-constrained version, on which LGM2026 relies (see Section 2), this variant incorporates a topography-based constraint after degree 600 and thus is more accurate in this spectral band. To conduct a spectral validation, we have harmonically analyzed the LGM2026 maps on the circumscribing sphere up to degree 11,519 (see Text S5.1 in Supporting Information). The differences between LGM2026 and GRGM1200B are shown in Figure 2. In low degrees up to 500, LGM2026 closely follows GRGM1200B as expected thanks to the low-frequency RTM correction (see Text S4 in Supporting Information). Even though LGM2026 relies exclusively on the Kaula-constrained GRGM1200B up to degree 500, the 2 models are not identical in this band probably because of the interpolation that was necessary to harmonically analyze LGM2026 (see Texts S4 and S5.1 in Supporting Information). Still, the discrepancies are below the formal errors of GRGM1200B. Beyond degree 500, the difference degree amplitudes between LGM2026 and GRGM1200B

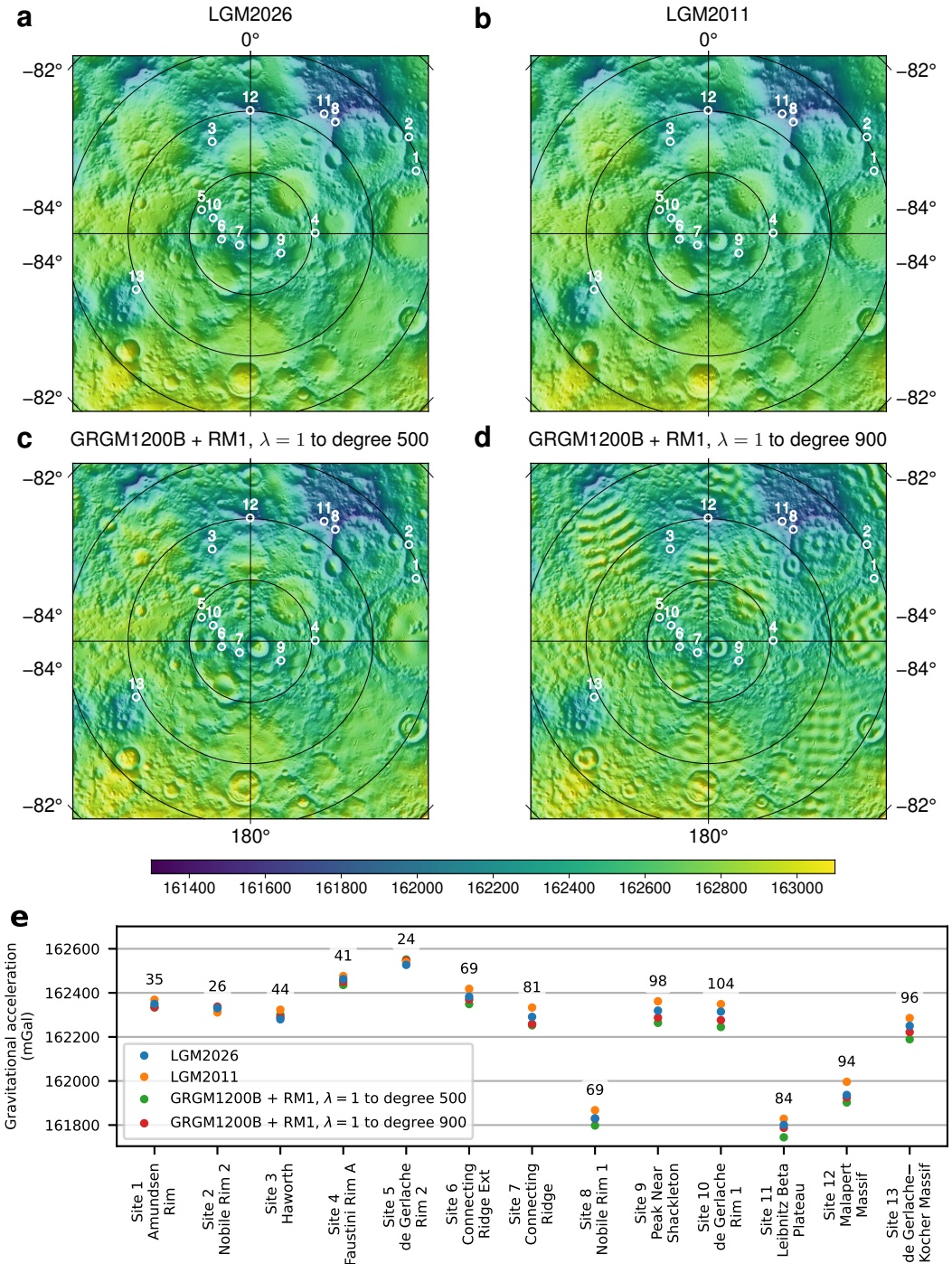


**Figure 1.** Gravitational acceleration (mGal) over the south polar region from LGM2026 (a), LGM2011 (b) and GRGM1200B + RM1, $\lambda = 1$ to degrees 500 (c) and 900 (d). LGM2011 is plotted in the Mean-Earth/Polar-Axis coordinate system while the remaining maps use the PA coordinates. The 13 points represent candidate Artemis locations for possible human landing (coordinates taken from S. J. Goossens et al., 2025, and transformed to PA for LGM2026 and GRGM1200B). LGM2026 and LGM2011 are not shown in their full resolution due to the size of the plotted area (see Figure S16 in Supporting Information for smaller region maps in full resolution). (e) Gravitational acceleration at the 13 stations. The values above the dots indicate the maximum differences between the predictions in mGal. The centrifugal acceleration was removed from LGM2011 to get the gravitational acceleration (Hirt & Featherstone, 2012).

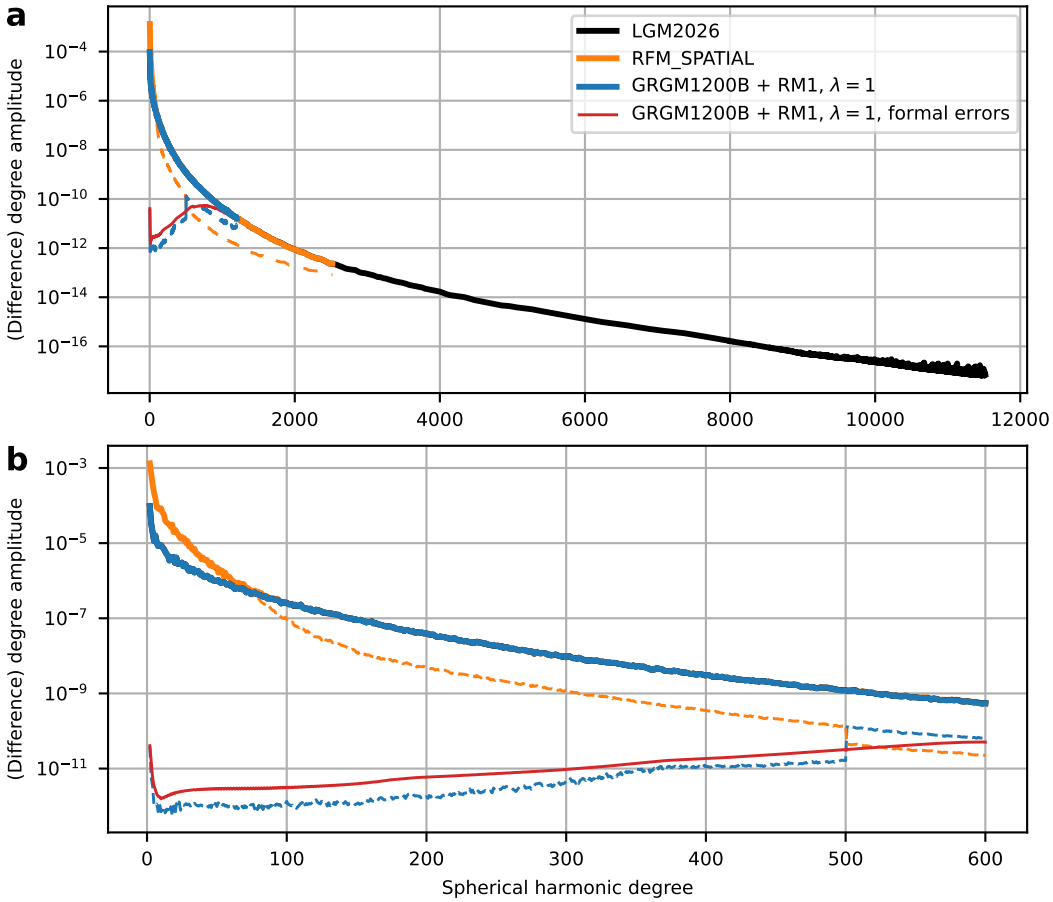


**Figure 2.** (a) Dimensionless degree amplitudes of LGM2026, GRGM1200B + RM1, $\lambda = 1$, and RFM_SPATIAL (thick lines) and their differences with respect to LGM2026 (thin dashed lines). The thin red line represents formal errors of GRGM1200B + RM1, $\lambda = 1$ that were published along with that model. Harmonic degrees 0 and 1 are omitted from the plot for better visualisation. All coefficients were rescaled to the same scaling constants and all degree amplitudes refer to the sphere of the radius 1749 km which passes outside the Moon in mass-free space. (b) Zoom-in to harmonic degrees 2 – 600.

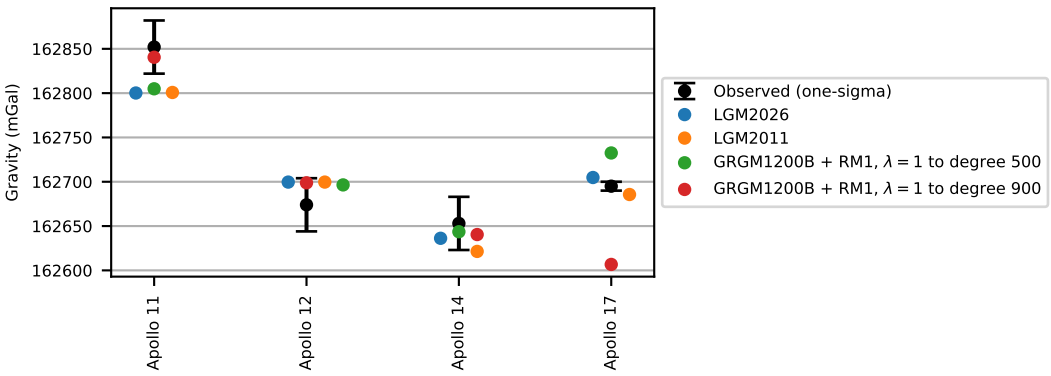


**Figure 3.** Gravity predictions at the Apollo sites compared to the observed gravity. The centrifugal acceleration was added to LGM2026 and to GRGM1200B + RM1, $\lambda = 1$ using the angular velocity $\omega = 2.6617073 \times 10^{-6}$ rad s$^{-1}$ (Wieczorek, 2015). The observed gravity values, their uncertainties and the site coordinates were taken from Hirt and Featherstone (2012). For LGM2026 and GRGM1200B, the coordinates were transformed to the PA coordinate system. Some of the dots are off-centered in the horizontal direction for visualization purposes.

experience a sudden jump, likely due to the missing GRAIL gravity observations in LGM2026 after degree 500. Beyond degree, say, 700 or 800, validation of LGM2026 with respect to GRGM1200B faces limitations due to the noise in GRGM1200B (see the red curve approaching the signal in Figure 2a). At these high degrees, LGM2026 can be compared with respect to RFM_SPATIAL (Šprlák et al., 2020), which is a degree-2519 model derived by gravity-forward modeling of the lunar crust using LOLA topography and a 3D density model. In long wavelengths (degrees below a few hundreds), LGM2026 expectedly does not match RFM_SPATIAL, because RFM_SPATIAL does not reflect the masses below the lunar crust. But in higher degrees, where the gravitational field of the lunar crust dominates in LGM2026, the 2 models agree reasonably well. Beyond degree 2519, LGM2026 remains unvalidated because of the lack of higher-degree spherical-harmonic lunar gravitational models. It is evident though that after degree ∼8500, noise overwhelms the signal (note that this holds only for the LGM2026 maps on the circumscribing sphere and not for the LGM2026 surface maps, see Text S5.1 in Supporting Information).

At the lunar surface, the accuracy assessment is limited by the scarcity of surface gravity observations. Available validation data consist of 4 surface gravity values determined by the Apollo 11, 12, 14 and 17 missions. The topography near the Apollo 11, 12 and 14 sites is mostly flat, resulting only in small variations of the gravitational field in these regions. When combined the large uncertainties of 30 mGal, the limitations of the validation at these 3 sites are clear. Conversely, the Apollo 17 site is located in a more rugged valley and the uncertainty of the gravity is reduced to 5 mGal. Figure 3 compares gravity predictions by LGM2026, LGM2011 and GRGM1200B to the observed gravity. All predictions fall within the two-sigma uncertainties except for the Apollo 17 site, where only LGM2026 and LGM2011 satisfy the two-sigma criterion. Notably, the Apollo 17 site happens to be the most suitable site for the validation due to its complex topography and low gravity uncertainty. Although our validation with respect to gravity from Apollo missions evidently lacks robustness, LGM2026 seem to be in agreement with existing models and especially with LGM2011.

An error analysis of the individual constituents of LGM2026 is provided in Texts S5.2, S5.3 and S5.4 in Supporting Information. By error propagation of the obtained uncertainties (the 90th percentile), the accuracy of the surface LGM2026 maps is estimated

to 13 $m^2$ $s^{-2}$ for the gravitational potential, 2 mGal for the gravitational vector, 220 E for the diagonal tensor elements and a few tens of E for the off-diagonal tensor elements (1 E = $10^{-9}$ $s^{-2}$). Near rims of craters and over rugged topography or LDEM128 artifacts (see Text S5.7 in Supporting Information), worse accuracy should be expected for the gravitational vector and especially for the gravitational tensor. The bulk of the 13 $m^2$ $s^{-2}$ error of the gravitational potential is due to the uncertainty of the vertical position of the LGM2026 surface grid. Therefore, if the normal gravitational potential is subtracted from the LGM2026 gravitational potential, the uncertainty of the disturbing potential will be about 3 to 4 orders of magnitude better compared to the gravitational potential. This is relevant, for instance, when computing the lunar geoid or quasigeoid. On the other hand, the uncertainties of the gravitational vector and tensor reflect mostly errors of our spatial-domain gravity-forward modeling and errors of the topography model LDEM128. Therefore, uncertainties of the disturbing field quantities derived from the gravitational vector (e.g., gravity anomaly or gravity disturbance) and from the gravitational tensor (e.g., the disturbing tensor) remain at the same levels as for the gravitational quantities, because other error sources dominate in this case. The errors of the LGM2026 grids on the circumscribing sphere are expected to be smaller than the errors at the lunar surface at least by 2 orders of magnitude for the gravitational potential, 1 orders of magnitude for the gravitational vector and 3 orders of magnitude for the gravitational tensor. This error reduction is due to the assumed deterministic radius of the circumscribing sphere as well as due to the increased distance from gravitating masses.

Finally, we compared LGM2026 and LGM2011 globally over the entire lunar surface (see Text S5.6 in Supporting Information). The discrepancies between the 2 models range from −220 to 203 mGal with the standard deviation of 23 mGal. Largest discrepancies are generally seen in long wavelengths, often over the mascons (see Figure S15 in Supporting Information). We attribute this mostly to the spherical-harmonic models representing long wavelengths in LGM2026 (the Kaula-constrained GRGM1200B to degree 500) and in LGM2011 (the pre-GRAIL model SGM100i to degree 70). Some discrepancies were also observed in short wavelengths which could be attributed to the different topography resolutions in LGM2026 and LGM2011 (128 PPD vs. 20 PPD). Overall, the observed standard deviation of 23 mGal falls within the declared uncertainties of LGM2026 (a few mGal) and LGM2011 (a few tens of mGal; Hirt & Featherstone, 2012).

## 6 Applications

LGM2026 could be beneficial to theoretical studies as well as practical engineering applications. *The maps of the gravitational potential* can help to establish a physically meaningful lunar height system (Tenzer et al., 2018) to study, for instance, gravity-driven mass movements or basalt flow direction (Wieczorek, 2015). *The maps of the gravitational vector* can be useful for gravity predictions at prospective landing sites, inertial navigation (Zemba et al., 2024), to verify/calibrate readings of accelerometers or to derive quantities such as gravity anomalies or deflections of the vertical. *The maps of the gravitational tensor* can be used for autonomous navigation of spacecraft based on gravity gradient measurements (Chen et al., 2023) or for upward/downward continuation of the gravitational potential and vector in mass-free space. *Maps on the circumscribing sphere* can be helpful for studying spectral properties of the lunar external gravitational field to ∼250-m spatial scales or for combining with the surface maps to radially interpolate the lunar gravitational field. Considering the synthesis of spherical-harmonic gravity models is a routine task, users can readily use *the residual gravitational maps* to supplement long wavelengths (harmonics up to degree 500) also from spherical-harmonic models other than GRGM1200B. *Spherical-harmonic coefficients of the gravitational potential to degree* 11,519 can be useful for studying the lunar gravitational field at fine scales in the spectral domain, to study convergence/divergence of spherical harmonics at the

lunar surface or to check/derive empirical power rules for the spectrum of the gravitational field of the Moon.

## 7 Limitations

Short-scale LGM2026 signals (beyond degree 500, wavelengths smaller than ∼11 km at the equator) do not rely on observed gravity but instead on gravity modeled from topography and density. Therefore, LGM2026 must not be geophysically or geologically interpreted at these scales.

Noise is present in the grids of the gravitational potential, the gravitational vector and the gravitational tensor on the circumscribing sphere at spatial scales smaller than ∼9 km (beyond degree 600), ∼2 km (beyond degree 2500) and ∼650 m (beyond degree 8500), respectively (see Text S5.1 in Supporting Information). This seems to be caused by the combination of the attenuated gravitational field and by the limited accuracy of our gravity-forward modeling in the spatial domain. The surface grids are not affected by this issue, because the short-scale gravitational signals are much stronger at the lunar surface (see Figure S12 in Supporting Information).

LDEM128 errors such as spikes or stripes (see Text S5.7 in Supporting Information) propagated into LGM2026 through the vertical position of evaluation points and through RTM. Visual screening of LGM2026 suggests the artifacts are found mostly (but not only) in latitudes $|\varphi| > 60°$.

## 8 Conclusions

LGM2026 are maps of the lunar gravitational field showing the gravitational potential, vector and tensor at the lunar surface and on its circumscribing sphere at the spatial resolution of 128 PPD (∼250 m at the equator). The maps combine GRAIL gravity (wavelengths up to ∼11 km at the equator) with gravity obtained by forward modeling of the LRO and Kaguya topography and 3D crustal density (scales smaller than ∼11 km). Besides the gravitational maps, LGM2026 provides an external spherical-harmonic expansion of the lunar gravitational field up to degree 11,519. To avoid divergence of spherical harmonics, the series should only be evaluated above the minimum sphere completely encompassing the Moon. Otherwise, it should be truncated appropriately based on a prior analysis. The accuracy of LGM2026 is estimated to 2 mGal at the lunar surface in terms of the gravitational vector. LGM2026 is freely available under the open CC BY 4.0 license.

This study can also be viewed as a proposal and validation of a methodology for high-resolution gravity field modeling near planetary surfaces using 3D density models. This task is challenging, because the numerically efficient spherical-harmonic methods are generally invalid at planetary surfaces due to the divergence issue. On the other hand, spatial-domain methods such as prisms or tesseroids are valid in the entire 3D space, but they require massive parallelization to employ them globally at high resolutions. Our approach modifies the spherical-harmonic method and combines it with existing spatial-domain methods to retain the accuracy and efficiency even at planetary surfaces. Once 3D variable density models of the Earth's topographic masses become available (Sheng et al., 2023), this framework is applicable also to the Earth's gravitational field.

## Conflict of Interest

The author declares there are no conflicts of interest for this manuscript.

## Data Availability Statement

The Lunar Gravitational Maps 2026 (LGM2026) are available at `https://misc.blazejbucha.com/lgm2026`. The lunar topography model LDEM128_PA_pixel_202405 (Neumann, 2024) is available at `https://pgda.gsfc.nasa.gov/products/95`. The spherical-harmonic model of the lunar topography Moon_LDEM128_shape_pa_11519.sh.gz (Wieczorek, 2024) is available at `https://zenodo.org/records/11533784`. The density model of the lunar crust LIN_L250-650_TC40_rho.grd and LIN_L250-650_TC40_grad.grd (S. Goossens et al., 2020) is available at `https://pgda.gsfc.nasa.gov/products/75`. The spherical-harmonic models GRGM1200B (S. Goossens et al., 2020) are available at `https://pgda.gsfc.nasa.gov/products/75`. The Lunar Gravity Model 2011 (LGM2011; Hirt & Featherstone, 2012) is available at `http://ddfe.curtin.edu.au/models/LGM2011`.

## Acknowledgments

Funded by the EU NextGenerationEU through the Recovery and Resilience Plan for Slovakia under the project No. 09I03-03-V04-00273. Part of the research results was obtained using the computational resources procured in the national project National competence centre for high performance computing (project code: 311070AKF2) funded by European Regional Development Fund, EU Structural Funds Informatization of society, Operational Program Integrated Infrastructure. We thank the HPC centre at the Slovak University of Technology in Bratislava, which is a part of the Slovak Infrastructure of High Performance Computing (SIVVP project, ITMS code 26230120002, funded by the European region development funds, ERDF). The maps were produced using the Generic Mapping Tools (Wessel et al., 2019). The plots were prepared with the Python's Matplotlib module (Hunter, 2007).

## References

Balmino, G., Vales, N., Bonvalot, S., & Briais, A. (2012). Spherical harmonic modelling to ultra-high degree of Bouguer and isostatic anomalies. *Journal of Geodesy*, *86*, 499–520. doi: 10.1007/s00190-011-0533-4

Barker, M. K., Mazarico, E., Neumann, G. A., Zuber, M. T., Haruyama, J., & Smith, D. E. (2016). A new lunar digital elevation model from the Lunar Orbiter Laser Altimeter and SELENE Terrain Camera. *Icarus*, *273*, 346–355. doi: 10.1016/j.icarus.2015.07.039

Barthelmes, F. (2013). *Definition of functionals of the geopotential and their calculation from spherical harmonic models: Theory and formulas used by the calculation service of the International Centre for Global Earth models (ICGEM), http://icgem.gfz-potsdam.de* (Scientific Technical Report No. STR09/02). Potsdam, Germany: GFZ German Research Centre for Geosciences. doi: 10.2312/GFZ.b103-0902-26

Besserer, J., Nimmo, F., Wieczorek, M. A., Weber, R. C., Kiefer, W. S., McGovern, P. J., ... Zuber, M. T. (2014). GRAIL gravity constraints on the vertical and lateral density structure of the lunar crust. *Geophysical Research Letters*, *41*, 5771–5777. doi: 10.1002/2014GL060240

Bucha, B. (2022). Spherical harmonic synthesis of area-mean potential values on irregular surfaces. *Journal of Geodesy*, *96*(68). doi: 10.1007/s00190-022-01658-1

Bucha, B. (2025). Spectral gravity forward modelling of 3D variable densities using an arbitrary integration radius with application to lunar topographic masses. *Journal of Geodesy*, *99*(31). doi: 10.1007/s00190-025-01951-9

Bucha, B., Hirt, C., & Kuhn, M. (2019). Cap integration in spectral gravity forward modelling: near- and far-zone gravity effects via Molodensky's truncation coefficients. *Journal of Geodesy*, *93*, 65–83. doi: 10.1007/s00190-018-1139-x

Bucha, B., & Kuhn, M. (2020). A numerical study on the integration radius separating convergent and divergent spherical harmonic series of topography-implied gravity. *Journal of Geodesy*, *94*, 112. doi: 10.1007/s00190-020-01442-z

Bucha, B., & Sansò, F. (2021). Gravitational field modelling near irregularly shaped bodies using spherical harmonics: a case study for the asteroid (101955) Bennu. *Journal of Geodesy*, *95*, 56. doi: 10.1007/s00190-021-01493-w

Chen, P., Mao, X., Sun, X., & Lai, Y. (2023). Autonomous navigation for lunar final approach based on gravity gradient measurements. *Advances in Space Research*, *71*, 1769–1783. doi: 10.1016/j.asr.2022.09.056

Chin, G., Brylow, S., Foote, M., Garvin, J., Kasper, J., Keller, J., ... Zuber, M. (2007). Lunar Reconnaissance Orbiter overview: the instrument suite and mission. *Space Science Reviews*, *129*, 391–419. doi: 10.1007/s11214-007-9153-y

Driscoll, J. R., & Healy, D. M. (1994). Computing Fourier transforms and convolutions on the 2-sphere. *Advances in Applied Mathematics*, *15*, 202–250.

Ďuríčková, Z., & Janák, J. (2016). RTM-based omission error corrections for global geopotential models: case study in Central Europe. *Studia Geophysica et Geodaetica*, *60*, 622–643. doi: 10.1007/s11200-015-0598-2

Fisher, E. A., Lucey, P. G., Lemelin, M., Greenhagen, B. T., Siegler, M. A., Mazarico, E., ... Zuber, M. T. (2017). Evidence for surface water ice in the lunar polar regions using reflectance measurements from the Lunar Orbiter Laser Altimeter and temperature measurements from the Diviner Lunar Radiometer experiment. *Icarus*, *292*, 74–85. doi: 10.1016/j.icarus.2017.03.023

Forsberg, R., & Tscherning, C. C. (1981). The use of height data in gravity field approximation by collocation. *Journal of Geophysical Research*, *86*, 7843–7854. doi: 10.1029/JB086iB09p07843

Goossens, S., Matsumoto, K., Liu, Q., Kikuchi, F., Sato, K., Hanada, H., ... Chen, M. (2011). Lunar gravity field determination using SELENE same-beam differential VLBI tracking data. *Journal of Geodesy*, *85*, 205–228. doi: 10.1007/s00190-010-0430-2

Goossens, S., Sabaka, T. J., Wieczorek, M. A., Neumann, G. A., Mazarico, E., Lemoine, F. G., ... Zuber, M. T. (2020). High-resolution gravity field models from GRAIL data and implications for models of the density structure of the Moon's crust. *Journal of Geophysical Research: Planets*, *125*, e2019JE006086. doi: 10.1029/2019JE006086

Goossens, S. J., Smith, D. E., Zuber, M. T., & Head, J. W. (2025). Shallow crustal density in the lunar south polar region. *The Planetary Science Journal*, *6*, 191. doi: 10.3847/PSJ/adf05f

Górski, K. M., Bills, B. G., & Konopliv, A. S. (2018). A high resolution Mars surface gravity grid. *Planetary and Space Science*, *160*, 84–106. doi: 10.1016/j.pss.2018.03.015

Grombein, T., Seitz, K., & Heck, B. (2017). On high-frequency topography-implied gravity signals for a height system unification using GOCE-based global geopotential models. *Surveys in Geophysics*, *38*, 443–477. doi: 10.1007/s10712-016-9400-4

Han, S. C., Schmerr, N., Neumann, G., & Holmes, S. (2014). Global characteristics of porosity and density stratification within the lunar crust from GRAIL gravity and Lunar Orbiter Laser Altimeter topography data. *Geophysical Research Letters*, *41*, 1882–1889. doi: 10.1002/2014GL059378

Hirt, C. (2012). Efficient and accurate high-degree spherical harmonic synthesis of gravity field functionals at the Earth's surface using the gradient approach. *Journal of Geodesy*, *86*, 729–744. doi: 10.1007/s00190-012-0550-y

Hirt, C., Bucha, B., Yang, M., & Kuhn, M. (2019). A numerical study of residual terrain modelling (RTM) techniques and the harmonic correction using ultra-high-degree spectral gravity modelling. *Journal of Geodesy*, *93*, 1469–1486. doi: 10.1007/s00190-019-01261-x

Hirt, C., Claessens, S., Fecher, T., Kuhn, M., Pail, R., & Rexer, M. (2013). New ultrahigh-resolution picture of Earth's gravity field. *Geophysical Research Letters*, *40*, 4279–4283. doi: 10.1002/grl.50838

Hirt, C., Claessens, S. J., Kuhn, M., & Featherstone, W. E. (2012). Kilometer-resolution gravity field of Mars: MGM2011. *Planetary and Space Science*, *67*, 147–154. doi: 10.1016/j.pss.2012.02.006

Hirt, C., & Featherstone, W. E. (2012). A 1.5 km-resolution gravity field model of the Moon. *Earth and Planetary Science Letters*, *329–330*, 22-30. doi: 10.1016/j.epsl.2012.02.012

Hirt, C., & Kuhn, M. (2014). Band-limited topographic mass distribution generates full-spectrum gravity field: Gravity forward modeling in the spectral and spatial domains revisited. *Journal of Geophysical Research: Solid Earth*, *119*, 3646–3661. doi: 10.1002/2013JB010900

Hirt, C., & Kuhn, M. (2017). Convergence and divergence in spherical harmonic series of the gravitational field generated by high-resolution planetary topography—A case study for the Moon. *Journal of Geophysical Research: Planets*, *122*, 1727–1746. doi: 10.1002/2017JE005298

Hirt, C., Kuhn, M., Claessens, S., Pail, R., Seitz, K., & Gruber, T. (2014). Study of the Earth's short-scale gravity field using the ERTM2160 gravity model. *Computers and Geosciences*, *73*, 71–80. doi: 10.1016/j.cageo.2014.09.001

Hirt, C., Reußner, E., Rexer, M., & Kuhn, M. (2016). Topographic gravity modeling for global Bouguer maps to degree 2160: Validation of spectral and spatial domain forward modeling techniques at the 10 microgal level. *Journal of Geophysical Research: Solid Earth*, *121*, 6846–6862. doi: 10.1002/2016JB013249

Hirt, C., Yang, M., Kuhn, M., Bucha, B., Kurzmann, A., & Pail, R. (2019). SRTM2gravity: an ultrahigh resolution global model of gravimetric terrain corrections. *Geophysical Research Letters*, *46*, 4618–4627. doi: 10.1029/2019GL082521

Hofmann-Wellenhof, B., & Moritz, H. (2005). *Physical Geodesy*. Wien, New York: Springer.

Hu, X., & Jekeli, C. (2015). A numerical comparison of spherical, spheroidal and ellipsoidal harmonic gravitational field models for small non-spherical bodies: examples for the Martian moons. *Journal of Geodesy*, *89*, 159–177. doi: 10.1007/s00190-014-0769-x

Hunter, J. D. (2007). Matplotlib: A 2D graphics environment. *Computing in Science & Engineering*, *9*, 90–95. (10.1109/MCSE.2007.55)

Ince, E. S., Abrykosov, O., Förste, C., & Flechtner, F. (2020). Forward gravity modelling to augment high-resolution combined gravity field models. *Surveys in Geophysics*, *41*, 767–804. doi: 10.1007/s10712-020-09590-9

Jekeli, C. (2017). *Spectral methods in geodesy and geophysics*. CRC Press.

Kato, M., Sasaki, S., Takizawa, Y., & the Kaguya project team. (2010). The Kaguya mission overview. *Space Science Reviews*, *154*, 3–19. doi: 10.1007/s11214-010-9678-3

Li, F., Yan, J., Xu, L., Shuanggen, J., Rodriguez, J. A. P., & Dohm, J. H. (2015). A 10 km-resolution synthetic Venus gravity field model based on topography. *Icarus*, *247*, 103–111. doi: 10.1016/j.icarus.2014.09.052

Lin, M., Denker, H., & Müller, J. (2020). Gravity field modeling using tesseroids with variable density in the vertical direction. *Surveys in Geophysics*, *41*, 723–765. doi: 10.1007/s10712-020-09585-6

Martinec, Z., & Einšpigel, D. (2018). SHAVEL: A program for the spherical harmonic analysis of a horizontal vector field sampled in an equiangular grid on a sphere. *Computer Physics Communications*, *233*, 206–214. doi: 10.1016/j.cpc.2018.06.015

McClanahan, T. P., Parsons, A. M., Livengood, T. A., Su, J. J., Chin, G., Hamara, D., ... Starr, R. D. (2024). Evidence for widespread hydrogen sequestration

within the Moon's south pole cold traps. *The Planetary Science Journal*, *5*, 217. doi: 10.3847/PSJ/ad5b55

Neumann, G. A. (2024). *LOLA MOON_PA gridded dataset [Data set]. NASA Goddard Space Flight Center Planetary Geodesy Data Archive.* doi: 10.60903/LOLA_PA

Pavlis, N. K., Holmes, S. A., Kenyon, S. C., & Factor, J. K. (2012). The development and evaluation of the Earth Gravitational Model 2008 (EGM2008). *Journal of Geophysical Research*, *117(B04406)*, 1–38. doi: 10.1029/2011JB008916

Pollack, H. N. (1973). Spherical harmonic representation of the gravitational potential of a point mass, a spherical cap and a spherical rectangle. *Journal of Geophysical Research*, *78*, 1760-1768. doi: 10.1029/JB078i011p01760

Rexer, M. (2017). *Spectral solutions to the topographic potential in the context of high-resolution global gravity field modelling* (Unpublished doctoral dissertation). Technische Universität München, München, Germany.

Rexer, M., Hirt, C., Bucha, B., & Holmes, S. (2018). Solution to the spectral filter problem of residual terrain modelling (RTM). *Journal of Geodesy*, *92*, 675–690. doi: 10.1007/s00190-017-1086-y

Sabaka, T. J., Nicholas, J. B., Goossens, S., Lemoine, F. G., & Mazarico, E. (2014). *Error propagation for high-degree gravity models developed from the GRAIL mission.* `https://pds-geosciences.wustl.edu/grail/grail-l-lgrs-5-rdr-v1/grail_1001/extras/clones/clone_description.pdf`, (accessed October 02, 2025).

Sansò, F. (2013). Harmonic Calculus and Global Gravity Models. In F. Sansò & M. G. Sideris (Eds.), *Geoid determination: Theory and methods* (pp. 111–168). Berlin, Heidelberg: Springer-Verlag.

Sheng, M., Shaw, C., & Kingdon, R. (2023). *Towards UNB_TopoDens version 3.0: The first global 3D topographical density model.* Retrieved from `https://doi.org/10.57757/IUGG23-3164` (XXVIII General Assembly of the International Union of Geodesy and Geophysics (IUGG) (Berlin 2023))

Šprlák, M., & Han, S.-C. (2021). On the use of spherical harmonic series inside the minimum Brillouin sphere: theoretical review and evaluation by GRAIL and LOLA satellite data. *Earth-Science Reviews*, *222*, 103739. doi: 10.1016/j.earscirev.2021.103739

Šprlák, M., Han, S.-C., & Featherstone, W. E. (2020). Crustal density and global gravitational field estimation of the Moon from GRAIL and LOLA satellite data. *Planetary and Space Sciences*, *192*, 105032. doi: 10.1016/j.pss.2020.105032

Tenzer, R., Foroughi, I., Sjöberg, L. E., Bagherbandi, M., Hirt, C., & Pitoňák, M. (2018). Definition of physical height systems for telluric planets and moons. *Surveys in Geophysics*, *39*, 313–335. doi: 10.1007/s10712-017-9457-8

Tiesinga, E., Mohr, P. J., Newell, D. B., & Taylor, B. N. (2021). CODATA recommended values of the fundamental physical constants: 2018. *Reviews of Modern Physics*, *93*. doi: 10.1103/RevModPhys.93.025010

Torge, W., & Müller, J. (2012). *Geodesy* (4th ed.). Berlin: Walter de Gruyter. doi: 10.1515/9783110250008

Tziavos, I. N., & Sideris, M. G. (2013). Topographic Reductions in Gravity and Geoid Modelling. In F. Sansò & M. G. Sideris (Eds.), *Geoid determination: Theory and methods* (pp. 337–400). Berlin, Heidelberg: Springer-Verlag.

Way, D. W. (2013). Preliminary assessment of the Mars Science Laboratory entry, descent, and landing simulation. In *2013 IEEE Aerospace conference.* Big Sky, MT, USA: IEEE. doi: 10.1109/AERO.2013.6497404

Wessel, P., Luis, J. F., Uieda, L., Scharroo, R., Wobbe, F., Smith, W. H. F., & Tian, D. (2019). The Generic Mapping Tools Version 6. *Geochemistry, Geophysics, Geosystems*, *20*, 5556–5564. doi: 10.1029/2019GC008515

Wieczorek, M. A. (2015). Gravity and topography of the terrestrial planets. In

G. Schubert (Ed.), *Treatise on geophysics* (2nd ed., pp. 153–193). Elsevier. doi: 10.1016/B978-0-444-53802-4.00169-X

Wieczorek, M. A. (2024). *Spherical harmonic models of the shape of the Moon (principal axis coordinate system) [LDEM128] (1.0.0) [Data set].* doi: 10.5281/zenodo.11533784

Wieczorek, M. A., Neumann, G. A., Nimmo, F., Kiefer, W. S., Taylor, G. J., Melosh, H. J., ... Zuber, M. T. (2013). The crust of the Moon as seen by GRAIL. *Science*, *339*, 671–675. doi: 10.1126/science.1231530

Williams, J. G., Konopliv, A. S., Boggs, D. H., Park, R. S., Yuan, D.-H., Lemoine, F. G., ... Zuber, M. T. (2014). Lunar interior properties from the GRAIL mission. *Journal of Geophysical Research: Planets*, *119*, 1546–1578. doi: 10.1002/2013JE004559

Zemba, M. J., Vaden, K. R., Reinhart, R., Gramling, C. J., & Heckler, G. W. (2024). *NASA's lunar communications and navigation architecture: human lunar return.* `https://ntrs.nasa.gov/citations/20230016359`.

Zuber, M. T., Smith, D. E., Watkins, M. M., Asmar, S. W., Konopliv, A. S., Lemoine, F. G., ... Yuan, D.-N. (2013). Gravity field of the Moon from the Gravity Recovery and Interior Laboratory (GRAIL) mission. *Science*, *339*, 668–671. doi: 10.1126/science.1231507